PAPER

Check for updates

Near-infrared emissive mononuclear lanthanide(III) complexes based on chiral Schiff base ligands: synthesis, crystal structure, luminescence, and magnetic properties

Yuri Jeong, [ID] [a] Ngoc Tram Anh Le,[b] Jeyun Ju,[b] Iuliia Olshevskaia,[b] Daeheum Cho,[b] Ryuya Tokunaga,[c] Shinya Hayami [ID] [c] and Kil Sik Min [ID] *[a]

In this study, novel chiral mononuclear complexes (teaH)[Ln((*R,R*)-dnsalcd)$_2$] (Ln = Nd^{3+} (**1**), Ho^{3+} (**2**), Er^{3+} (**3**), Yb^{3+} (**4**), and Gd^{3+} (**5**)), where teaH = triethylammonium and (*R,R*)-H$_2$dnsalcd = (*R,R*)-*N,N'*-bis(3,5-dinitrosalicylidene)-1,2-cyclohexanediamine, were synthesized and characterized. Their structural features were analyzed *via* single-crystal diffraction, and their chiral and magnetic properties were examined through circular dichroism and magnetic susceptibility, respectively. Structural analysis revealed two distinct coordination modes: complexes **1** and **4** were isomorphous, each exhibiting a single intramolecular π–π stacking interaction, and complexes **3** and **5** were also isomorphous, each displaying two intramolecular π–π stacking interactions. Complexes **1** and **4** show strong near-infrared (NIR) emissions in both solid and solution states, attributed to efficient antenna effects. In contrast, complexes **2** and **3** exhibit weaker NIR emissions with Stark splitting features. Circular dichroism measurements confirmed the chiroptical activity of the complexes, and magnetic susceptibility data revealed typical lanthanide-type paramagnetic behavior. Density functional theory (DFT) calculations for complex **3** support a ligand-to-metal energy transfer mechanism, involving two sequential internal conversion processes.

Introduction

Lanthanide metal complexes exhibit unique properties, including sharp and long-lived emission peaks and large pseudo-Stokes shifts owing to the shielding of 4f electrons.[1–3] Over the decades, extensive research has explored their multifunctional technological applications in bioimaging, sensing, light-emitting diodes, and single-molecule magnets.[4–13] Among them, NIR-emitting lanthanide complexes can be used for applications in telecommunications, biosciences, and solar energy conversion.[14–17] Generally, lanthanide complexes with Nd(III), Ho(III), Er(III), and Yb(III) ions can exhibit NIR emissions between 900 nm and 1600 nm.[18,19] For instance, Pikramenou *et al.* reported Ln(tpOp)$_3$ (Ln = Nd, Er, and Yb) complexes featuring a tetraphenyl imidodiphosphonate ligand (HtpOp).[20] These complexes exhibit NIR luminescence with long life-times, ranging from 3.3 μs for Nd(tpOp)$_3$ to 20 μs for Yb

(tpOp)$_3$. Spodine *et al.* reported three Er(III) hexaazamacrocylic complexes—Er-EDA (EDA = ethylenediamine), Er-OPDA (OPDA = *ortho*-phenylenediamine), and Er-DAP (DAP = 1,3-diaminopropane).[21] Bluish-green and green emissions from the Er(III) ion upon ligand-centered excitation are observed only in complexes with macrocycles containing aliphatic spacers (Er-EDA and Er-DAP), whereas the complex with aromatic spacers (Er-OPDA) exhibits only ligand-based emission. This highlights the structural dependence of energy transfer from the ligand to the Er(III) emission levels.

Chiral metal complexes have been utilized as chiral catalysts and in chiral magnetism.[22,23] Particularly, in the case of chiral lanthanide(III) complexes, they can be applied for circularly polarized luminescence (CPL), due to their strong emissions.[24,25] Thus, it is quite important to design chiral ligands that can act as chiral luminophores. Recently, we have reported two mononuclear complexes (teaH)[Ln(dnsalcd)$_2$] with chiral ligands (*S,S/R,R*)-*N,N'*-bis(3,5-dinitrosalicylidene)-1,2-cyclohexanediamine ((*S,S/R,R*)-H$_2$dnsalcd), which exhibit unusual luminescence properties depending on the molecular geometry (Ln = Eu^{3+}, Tb^{3+}, teaH = triethylammonium).[26] The Eu(III) complex shows highly efficient red emission, whereas the Tb(III) complex displays no visible emission owing to differences in π–π stacking interactions. We have found that the

[a]Department of Chemistry Education and Science Education Research Institute, Kyungpook National University, Daegu 41566, Republic of Korea. E-mail: minks@knu.ac.kr
[b]Department of Chemistry, Kyungpook National University, Daegu 41566, Republic of Korea
[c]Department of Chemistry, Kumamoto University, Kumamoto 860-8555, Japan

photoluminescence properties of the lanthanide(III) complexes can be effectively tuned by the coordination modes of the dnsalcd^{2-} ligands.

In this context, our research has focused on the development of new lanthanide(III) complexes capable of exhibiting near-infrared (NIR) emissions. The chiral dnsalcd^{2-} ligand demonstrates a significant antenna effect, influenced by its coordination geometry—specifically, the energy transfer from the ligand to the lanthanide(III) ion and potential self-quenching within the ligand. Based on our preliminary findings, we anticipate that NIR emissions can be both induced and controlled in lanthanide(III) complexes formed through the reaction of chiral dnsalcd^{2-} ligands with lanthanide(III) ions, owing to the antenna effect of the coordinated ligands. Herein, the synthesis, crystal structure, circular dichroism, magnetic and luminescence properties of (teaH)[Ln^{III}((R,R)-dnsalcd)$_2$] (Ln = Nd (**1**), Ho (**2**), Er (**3**), Yb (**4**), and Gd (**5**)) are reported (Chart 1). Additionally, DFT calculations were performed to elucidate the emission mechanism.

Experimental

General

All chemicals used in this study were of reagent grade and used without further purification. (R,R)-N,N'-Bis(3,5-dinitrosalicylidene)-1,2-cyclohexanediamine ((R,R)-H$_2$dnsalcd) was synthesized as previously described.[26,27] Lanthanide salts containing nitrate or chloride anion were purchased from Sigma-Aldrich. Infrared (IR) spectra were measured using KBr pellets on a Thermo Fisher Scientific Nicolet iS5 spectrophotometer (±1 cm^{-1}). UV-vis absorption spectra were recorded using a SCINCO S-3100 spectrophotometer (solution and diffuse reflectance mode). X-ray powder diffraction patterns were measured using a 4 kW Empyrean instrument (Panalytical, Netherlands) with degree increments and time steps of 0.02° and 0.2 s per step at 2θ and room temperature. Elemental analyses were performed using a Fisons/Carlo Erba EA1108 instrument in the

air. ^{1}H NMR spectra were measured with a Bruker AVANCE III 500 spectrometer, while circular dichroism (CD) spectra were recorded using a Jasco 1500 spectropolarimeter. Temperature-dependent magnetic susceptibilities were measured using a Quantum Design MPMS-5S superconducting quantum interference device (SQUID) magnetometer in a 5000 Oe applied field from 2 to 300 K at a 2 K min^{-1} sweep rate. Diamagnetic corrections were made using Pascal's constants.[28] Luminescence spectra were recorded using a SCINCO FS-2 fluorescence spectrometer or a Horiba Fluorolog-3 spectrofluorometer equipped with a photomultiplier tube (PMT) detector. Luminescence spectra were recorded at multiple excitation wavelengths, which were selected based on the strongest UV-vis absorption peaks of each sample. Density functional theory (DFT) calculations were performed at the M062X theory level using the SARC2-ZORA-QZVP basis set for the Er(III) atom and the ZORA-def2-TZVP basis set for all other atoms.[29–33]

Syntheses of the compounds

(teaH)[Nd^{III}((R,R)-dnsalcd)$_2$] (1). A 5 mL dimethoxyethane solution of (R,R)-H$_2$dnsalcd (69 mg, 0.136 mmol) was mixed with triethylamine (28 mg, 0.272 mmol) at room temperature and stirred for 15 min, yielding a yellow solution. A methanol solution (2 mL) of neodymium(III) nitrate hydrate (30 mg, 0.068 mmol) was then added dropwise to the yellow solution and stirred for 10 min. The resulting mixture was filtered, and yellow diamond-shaped crystals were obtained through diethyl ether diffusion, collected *via* filtration, washed with diethyl ether, and air-dried. Yield: 63 mg (68%). Anal. calcd for C$_{46}$H$_{48}$N$_{13}$NdO$_{20}$: C, 44.30; H, 3.88; N, 14.60. Found: C, 44.61; H, 4.12; N, 14.18. FT-IR (KBr, cm^{-1}): 3084, 2936, 2861, 1632, 1596, 1561, 1529, 1328, 1099. UV/vis (in MeCN), λ_{max} (ε): 234 nm (7.3 × 10^4 M^{-1} cm^{-1}), 352 nm (7.7 × 10^4 M^{-1} cm^{-1}). UV/Vis (diffuse reflectance spectrum), λ_{max}: 200–550 nm (broad), 586 nm.

(teaH)[Ho^{III}((R,R)-dnsalcd)$_2$] (2). A 20 mL ethanol solution of (R,R)-H$_2$dnsalcd (116 mg, 0.232 mmol) was mixed with triethylamine (47 mg, 0.46 mmol) at room temperature and stirred for 15 min, yielding a yellow solution. A 5 mL ethanol solution of holmium(III) chloride hydrate (44 mg, 0.12 mmol) was then added, and the mixture was stirred for 10 min. The resulting yellow precipitate was then filtered, washed with ethanol, and air-dried. Yield: 136 mg (84%). Yellow diamond-shaped crystals of **2** suitable for X-ray crystallography were obtained by diffusing diethyl ether into a solution containing (R,R)-H$_2$dnsalcd and triethylamine in 1,2-dimethoxyethane and holmium(III) chloride hydrate in methanol for 3 days. Anal. calcd for C$_{46}$H$_{48}$HoN$_{13}$O$_{20}$: C, 43.58; H, 3.82; N, 13.36. Found: C, 43.46; H, 3.88; N, 13.63. IR (KBr, cm^{-1}): 3078, 2933, 2856, 1632, 1596, 1567, 1528, 1330, 1099. UV/vis (in MeCN), λ_{max} (ε): 234 nm (8.6 × 10^4 M^{-1} cm^{-1}), 352 nm (9.0 × 10^4 M^{-1} cm^{-1}). UV/vis (diffuse reflectance spectrum), λ_{max}: broad absorption (200–500 nm), peaks at 537 nm and 650 nm.

Synthesis of (teaH)[M^{III}((R,R)-dnsalcd)$_2$] (M = Er (3), Yb (4), and Gd (5))

A synthetic procedure similar to that of **2** was followed for the isolation of complexes **3–5**, but holmium(III) chloride hydrate
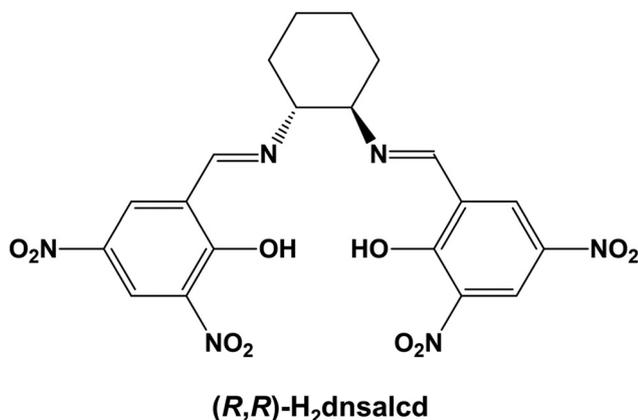

Chart 1 Structure of (R,R)-N,N'-bis(3,5-dinitrosalicylidene)-1,2-cyclohexanediamine in a tetradentate configuration.

was replaced with the corresponding lanthanide precursors erbium(III) nitrate hydrate (51 mg, 0.12 mmol), ytterbium(III) nitrate hydrate (44 mg, 0.12 mmol), and gadolinium(III) nitrate hydrate (52 mg, 0.12 mmol). All crystals of **3–5** suitable for X-ray crystallography were obtained by diffusing diethyl ether into a mixed solution of (R,R)-H$_2$dnsalcd and triethylamine in 1,2-dimethoxyethane and each metal nitrate hydrate in methanol for 3 days.

For **3**: Yield: 116 mg (74%). Anal. calcd for C$_{46}$H$_{48}$ErN$_{13}$O$_{20}$: C, 43.50; H, 3.81; N, 14.34. Found: C, 43.65; H, 3.77; N, 14.19. IR (KBr, cm^{-1}): 3085, 2935, 2860, 1634, 1596, 1588, 1529, 1332, 1101. UV/vis (in MeCN), λ_{max} (ε): 234 nm (8.6 × 10^4 M^{-1} cm^{-1}), 352 nm (8.8 × 10^4 M^{-1} cm^{-1}). UV/vis (diffuse reflectance spectrum), λ_{max}: 200–500 nm (broad), 519 nm, 659 nm.

For **4**: Yield: 113 mg (71%). Anal. calcd for C$_{46}$H$_{48}$N$_{13}$O$_{20}$Yb: C, 43.30; H, 3.79; N, 14.27. Found: C, 43.58; H, 3.54; N, 13.90. IR (KBr, cm^{-1}): 3080, 2935, 2857, 1633, 1596, 1567, 1529, 1331, 1100. UV/vis (in MeCN), λ_{max} (ε): 234 nm (7.0 × 10^4 M^{-1} cm^{-1}), 352 nm (7.2 × 10^4 M^{-1} cm^{-1}). UV/vis (diffuse reflectance spectrum), λ_{max}: 200–600 nm (broad).

For **5**: Yield: 101 mg (70%). Anal. calcd for C$_{46}$H$_{48}$GdN$_{13}$O$_{20}$: C, 43.84; H, 3.84; N, 14.45. Found: C, 43.59; H, 3.90; N, 14.20. IR (KBr, cm^{-1}): 3068, 2935, 2859, 1634, 1596, 1568, 1527, 1333, 1102. UV/vis (in MeCN), λ_{max} (ε): 234 nm (8.6 × 10^4 M^{-1} cm^{-1}), 351 nm (9.1 × 10^4 M^{-1} cm^{-1}). UV/vis (diffuse reflectance spectrum), λ_{max}: 200–600 nm (broad).

X-ray crystallographic data collection and refinement

Single crystals of **1–5** were mounted on a CryoLoop® with Paratone® oil. Intensity data were collected for all complexes at 223(2) K on the Bruker D8 VENTURE diffractometer equipped with a microfocus Mo-target X-ray tube (λ = 0.71073 Å) and a PHOTON 100 CMOS detector (Korea Basic Science Institute, Western Seoul Center). The data of **1–5** were processed using the Bruker APEX3 program,[34] while data reduction and integration were performed using the Bruker SAINT program (v8.40A) and absorption-corrected with SADABS.[35] Structure solutions were performed with direct methods using SHELXT-2014/5[36] and refined with a full-matrix least-squares approach in the SHELXL-2019/3 computer program.[37] Unfortunately, the structure of **2** has been omitted from this paper because of a significant issue in the F_{obs} versus F_{calc} plot, despite the fact that its crystal structure could be identified. The refinements of **3–5** were carried out using selected data cuts at 2θ = 46°, 43°, and 45°, respectively, to eliminate poor reflections and low-resolution data at higher 2θ angles. Due to the disorder observed in **1** and **3–5**, the structures were refined using disorder models. To achieve satisfactory refinement of the disordered benzene rings and NO$_2$ groups, a combination of constraints (EADP) and restraints (SAME, SADI, SIMU, DFIX, DANG, ISOR, and RIGU) was applied. In particular, refinement of the cation site in structure **4** was carried out using the PLATON squeeze option due to positional disorder.[38] The positions of all non-hydrogen atoms were refined with anisotropic displacement factors. All hydrogen atom positions were constrained to their parent atoms using the appropriate HFIX command in SHELXL-2019/3 and a riding model. Additionally, we have added the plots of R_{merge} and I/σ versus resolution of **1** and **3–5** (Fig. S1). Table 1 summarizes the crystallographic data and refinement results of the five complexes.

Table 1 Summary of the crystallographic data for **1** and **3–5**

Compound	1	3	4	5
Empirical formula	C$_{51}$H$_{62}$N$_{13}$NdO$_{22}$	C$_{46}$H$_{48}$ErN$_{13}$O$_{20}$	C$_{46}$H$_{48}$N$_{13}$O$_{20}$Yb	C$_{46}$H$_{48}$GdN$_{13}$O$_{20}$
Formula weight	1353.37	1270.23	1276.01	1260.22
Crystal system	Orthorhombic	Hexagonal	Tetragonal	Hexagonal
Space group	$P2_12_12_1$	$P6_1$	$P4_32_12$	$P6_1$
a (Å)	13.5169(12)	13.3689(16)	12.5403(9)	13.424(4)
b (Å)	19.006(2)	13.3689(16)	12.5403(9)	13.424(4)
c (Å)	22.585(3)	49.867(11)	35.322(4)	49.95(2)
α (°)	90	90	90	90
β (°)	90	90	90	90
γ (°)	90	120	90	120
V (Å^3)	5802.2(11)	7718(2)	5554.6(10)	7795(6)
Z	4	6	4	6
d_{calc} (g cm^{-3})	1.549	1.640	1.526	1.611
λ (Å)	0.71073	0.71073	0.71073	0.71073
T (K)	223(2)	223(2)	223(2)	223(2)
μ (mm^{-1})	0.985	1.723	1.769	1.367
$F(000)$	2780	3858	2580	3834
Reflections collected	42 223	19 248	11 757	20 845
Independent reflections	14 285	6651	3188	6632
Reflections with $I > 2\sigma(I)$	12 210	4837	2432	4646
Goodness-of-fit on F^2	1.017	1.004	1.012	0.987
Flack's parameter	−0.014(6)	−0.006(14)	−0.002(13)	−0.019(18)
R_1 [a] [$I > 2\sigma(I)$]	0.0379	0.0596	0.0533	0.0590
wR_2 [b] [$I > 2\sigma(I)$]	0.0654	0.0987	0.1182	0.1063
CCDC	2448369	2448371	2448372	2448373

[a] $R_1 = \sum ||F_o| - |F_c||/\sum |F_o|$. [b] $wR_2 = [\sum w(F_o^2 - F_c^2)^2/\sum w(F_o^2)^2]^{1/2}$.

Results and discussion

Synthesis and characterization

Mononuclear chiral complexes (teaH)[M^{III}((*R*,*R*)-dnsalcd)$_2$] (M = Nd (**1**); Ho (**2**); Er (**3**); Yb (**4**); Gd (**5**)) were obtained as yellow crystalline solids in good yields (68–84%) through the reaction of lanthanide salts with a tetradentate N$_2$O$_2$-type ligand. The synthesis involved mixing a lanthanide(III) salt, (*R*,*R*)-H$_2$dnsalcd, and triethylamine in a 1 : 2 : 4 molar ratio in ethanol (dimethoxyethane/methanol for **1**). For complex **1**, single crystals of (teaH)[Nd((*R*,*R*)-dnsalcd)$_2$] were obtained and utilized for all characterization processes. In contrast, solids **2–5** were prepared as precipitates, with their structures confirmed through powder X-ray diffraction (Fig. S2–S5). The IR spectrum of **1** exhibited the characteristic peaks of azomethine imine bonds at 1632 cm^{-1}, which were downshifted by *ca.* 22 cm^{-1} for the free (*R*,*R*)-H$_2$dnsalcd ligand (Fig. S6).[39] Additionally, peaks corresponding to benzene double bonds were downshifted to *ca.* 1596 cm^{-1} owing to coordination with Nd(III) ion.[26] The aromatic and aliphatic C–H bands of (*R*,*R*)-dnsalcd^{2-} and teaH$^+$ cations appear at *ca.* 3084, 2936, and 2861 cm^{-1}, respectively. Moreover, the band at 1328 cm^{-1} corresponds to the symmetric stretching vibrations of the nitro groups in (*R*,*R*)-dnsalcd^{2-}. Similarly, the IR spectra of **2–5** exhibited similar patterns, with slight wavenumber differences owing to coordination with different lanthanide(III) metal ions. Fig. S7 shows the UV-Vis spectra for the (*R*,*R*)-H$_2$dnsalcd ligand and complexes **1–5** in the solid state at room temperature. The spectra display broad absorption bands between 200 and 600 nm. Additionally, complexes **1–3** showed characteristic absorption peaks of lanthanide metal ions consistent with a previous report.[40] For complex **1**, the sharp peak was observed at 586 nm owing to the transition from the ground state $^4I_{9/2}$ to an emitting level $^4G_{5/2}$. Complex **2** displayed two absorption lines at 537 and 650 nm, attributed to the 4f–4f transitions of $^5I_8 \rightarrow {}^5F_4$ and $^5F_5$, respectively. Similarly, complex **3** showed two absorption bands at 519 and 649 nm, corresponding to $^4I_{15/2} \rightarrow {}^2H_{11/2}$ and $^4F_{9/2}$, respectively. In contrast, complexes **4** and **5** did not show any observable f–f transitions owing to strong ligand absorption.[41,42] However, their UV-Vis absorption spectra in solution have been measured in acetonitrile (Fig. S8). Two sharp absorption peaks were observed at 233 and 352(1) nm, as previously reported.[26] These peaks correspond to the $\pi \rightarrow \pi^*$ transitions of the phenolate and azomethine groups, respectively.

To examine the structural characteristics of optically active chiral compounds, CD spectra for the (*R*,*R*)-H$_2$dnsalcd and complexes **1–5** were obtained in an acetonitrile solution at room temperature (Fig. 1). The CD spectrum of (*R*,*R*)-H$_2$dnsalcd exhibited two positive Cotton effects at 270 and 390 nm and two negative Cotton effects at 250 and 434 nm. Upon ligand complexation with Ln(III) ions, the CD absorption peak at 434 nm, corresponding to charge transfer from the benzene to the nitro group, disappeared, as confirmed *via* the UV-Vis spectra (Fig. S8). The negative band observed at 271 and 276 nm for complexes **1** and **5**, respectively, indicates the π

→ π* transition of the ligand phenolic group. However, for complexes **2–4**, it splits into 246 nm and 283(1) nm, owing to the Stark effect (Fig. 1). Additionally, the positive and negative Cotton effects at 318–327 and 362–382 nm, respectively, were attributed to the π → π* transition of the azomethine groups in the (*R*,*R*)-dnsalcd^{2-} ligand.[26]

Description of the crystal structures

Structure of 1. Complex **1** crystallizes in the orthorhombic $P2_12_12_1$ space group. Fig. 2 shows the oak ridge thermal ellipsoid plot (ORTEP) representation of **1**, and Table 2 lists the selected bond lengths and angles. The asymmetric unit comprises a crystallographically independent Nd(III) complex anion with a teaH$^+$ cation and lattice solvent molecules (*i.e.*, one CH$_3$OH and one CH$_3$CH$_2$OCH$_2$CH$_3$). The Nd(III) cation is coordinated by four phenoxide ions and four nitrogen atoms from two (*R*,*R*)-dnsalcd^{2-} ligands, forming an N$_4$O$_4$ coordination environment with a distorted square-antiprismatic geometry (Table S1). The average Nd–N and Nd–O bond lengths were 2.627(2) and 2.377(2) Å, respectively. These differences reflect the different radii and strains of N and O.[43] Complex **1** showed an intramolecular π–π stacking interaction between the two phenoxide groups (O2a/O2b) of two (*R*,*R*)-dnsalcd^{2-} ligands. This is attributed to the severely distorted bonding of each (*R*,*R*)-dnsalcd^{2-} ligand to the Nd(III) core.[26] Furthermore, the centroid–centroid distance was 3.570 Å, with a dihedral angle of 17.5(2)° between the benzene rings, indicating slight distortion in the π–π stacking interaction (Fig. S9).[44]

Structure of 3. Complex **3** crystallized in the hexagonal $P6_1$ space group, and Fig. 3 shows its ORTEP representation, while Table 2 shows the selected bond lengths and angles. The asymmetric unit was composed of one Er(III) cation, two (*R*,*R*)-dnsalcd^{2-} ligands, and one teaH$^+$ cation, which served to balance the charge of the complex anion. That is, the central Er(III) ion was eight-coordinated, adopting a distorted square-antiprismatic geometry (Table S1). The average Er–N and Er–O bond distances were determined to be 2.525(7) and 2.273(6) Å, respectively. These differences were attributed to the different sizes and strains of N and O atoms.[43] Complex **3** showed two intramolecular π–π stacking interactions between the two phenoxide groups (O1a/O1b and O2a/O2b) of the two (*R*,*R*)-dnsalcd^{2-} ligands. This can be attributed to each (*R*,*R*)-dnsalcd^{2-} ligand binding to the Er(III) center in an overlapping mode, adopting a staggered conformation with a dihedral angle of 88.7(3)° through the coordinated N and O atoms.[26] Moreover, the centroid–centroid distances were found to be 3.486 and 3.508 Å, while the dihedral angles between the benzene rings were 7.6(5)° and 7.2(1.1)°, indicating slight distortions in the π–π stacking interactions (Fig. S9).[44]

Structure of 4. Complex **4** crystallized in the tetragonal $P4_32_12$ space group, and Fig. 4 shows its ORTEP representation, while Table 2 shows the selected bond lengths and angles. The asymmetric unit contained one crystallographically independent Yb(III) complex cation, present as a half complex, along with a half teaH$^+$ cation. Thus, the complex adopted a distorted square-antiprismatic geometry with a
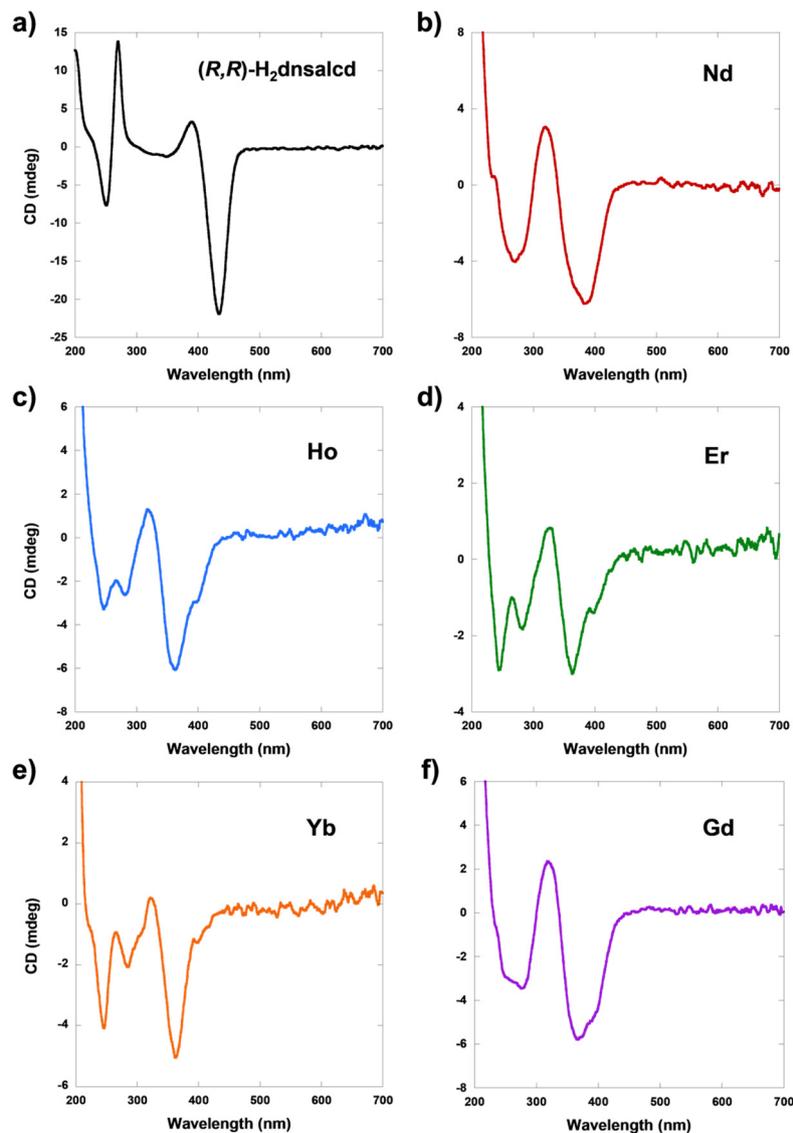
Fig. 1 CD spectra of (a) (R,R)-H$_2$dnsalcd, (b) Nd (**1**), (c) Ho (**2**), (d) Er (**3**), (e) Yb (**4**), and (f) Gd (**5**) in MeCN solutions at room temperature.

coordination number of 8, imposed by the symmetry operation. Although the triethylammonium cation was identified in the crystal structure, it was treated using the squeezing option owing to disorder. In the structure, the Yb(III) cation was coordinated to four phenoxide ions and four nitrogen atoms from two (R,R)-dnsalcd^{2-} ligands, resulting in an N$_4$O$_4$ coordination environment and a distorted square-antiprismatic geometry (Table S1). The average Yb–N and Yb–O bond distances were determined to be 2.498(7) and 2.241(5) Å, respectively. Likewise, these differences were related to the different atomic radii and strains of N and O atoms.[43] Complex **4** showed one intramolecular π–π stacking interaction between the two phenoxide groups (O1a/O1b) of the two (R,R)-dnsalcd^{2-} ligands, similar to what was observed in complex **1**. This can be attributed to each (R,R)-dnsalcd^{2-} ligand binding to the Yb(III) center in a highly distorted mode.[26] Moreover, the

centroid–centroid distance was found to be 3.723 Å, with a dihedral angle of 3.4(7)° between the benzene rings, indicating a slight distortion in the π–π stacking interaction (Fig. S9).[44] Each (R,R)-dnsalcd^{2-} ligand was also coordinated to the Yb(III) ion in a square planar mode, adopting a staggered conformation with a dihedral angle of 89.3(3)° through the coordinated N and O atoms.

Structure of 5. Complex **5** was isostructural with complex **3**, implying that it shared the same crystal system, space group, and asymmetric unit. Complex **5** crystallized in the hexagonal $P6_1$ space group, and Fig. 5 shows its ORTEP representation, while Table 2 shows the selected bond lengths and angles. The asymmetric unit was composed of one Gd(III) cation, two (R,R)-dnsalcd^{2-} ligands, and one teaH$^+$ cation, which served to balance the charge of complex anions. That is, the central Gd (III) ion was eight-coordinated, adopting a distorted square-
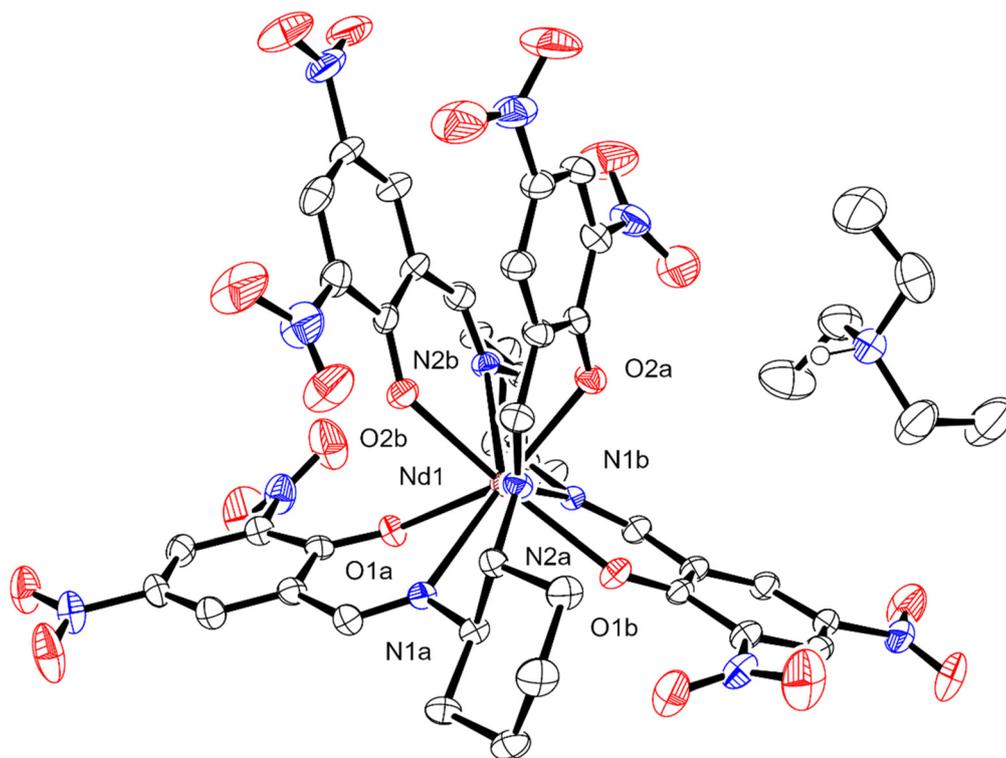
Fig. 2 ORTEP representation of complex **1**, with atoms represented by 50% probable thermal ellipsoids. All hydrogen atoms and solvent molecules are omitted for clarity, except the hydrogen atom on the nitrogen of the triethylammonium cation.

Table 2 Selected bond distances (Å) and angles (°) for **1** and **3–5**

Compound	**1**	**3**	**4**	**5**
Ln–N1a	2.599(4)	2.518(16)	2.525(13)	2.610(15)
Ln–N2a	2.649(3)	2.537(14)	2.471(13)	2.538(15)
Ln–N1b	2.582(4)	2.556(15)	2.525(13)	2.530(13)
Ln–N2b	2.662(4)	2.496(13)	2.471(13)	2.630(16)
Ln–O1a	2.367(3)	2.272(12)	2.254(10)	2.306(12)
Ln–O2a	2.390(3)	2.281(13)	2.225(11)	2.299(13)
Ln–O1b	2.395(3)	2.228(12)	2.254(10)	2.387(13)
Ln–O2b	2.356(3)	2.319(13)	2.225(11)	2.279(13)
O1a–Ln–O1b	116.53(11)	95.5(4)	104.4(6)	94.0(5)
O1a–Ln–O2b	81.12(12)	91.1(5)	84.7(4)	92.7(5)
O1a–Ln–O2a	152.66(11)	149.5(4)	152.3(4)	151.2(5)
O1a–Ln–N1a	68.51(11)	71.6(5)	70.0(4)	71.1(5)
O1a–Ln–N2a	126.06(11)	138.6(5)	133.8(4)	138.1(5)
O1a–Ln–N1b	82.79(12)	73.6(4)	73.0(4)	75.5(5)
O1a–Ln–N2b	81.19(11)	79.3(5)	76.0(4)	82.3(5)
O1b–Ln–O2a	87.40(11)	92.5(4)	84.7(4)	90.4(5)
O1b–Ln–O2b	154.99(13)	150.7(4)	152.3(4)	153.1(4)
O1b–Ln–N1a	84.94(12)	76.1(5)	73.0(4)	77.7(4)
O1b–Ln–N2a	80.79(11)	79.4(4)	76.0(4)	81.0(4)
O1b–Ln–N1b	69.83(12)	72.8(4)	70.0(4)	69.8(5)
O1b–Ln–N2b	128.06(11)	137.8(5)	133.8(4)	135.0(5)
N1a–Ln–N2a	62.50(12)	67.3(5)	66.1(4)	67.2(5)
N1a–Ln–N1b	127.81(12)	130.0(5)	117.6(6)	130.9(5)
N1a–Ln–N2b	143.52(12)	137.8(5)	141.7(4)	139.9(5)
N2a–Ln–N1b	146.48(12)	139.8(5)	141.7(4)	137.8(5)
N2a–Ln–N2b	129.81(11)	130.7(4)	136.9(7)	129.5(5)
N1b–Ln–N2b	64.45(12)	65.5(4)	66.1(4)	65.9(5)

antiprismatic geometry (Table S1). The average Gd–N and Gd–O bond distances were determined to be 2.572(7) and 2.317(6) Å, respectively. These differences were attributed to the different sizes and stains of the corresponding N and O atoms.[43] Complex **5** showed two intramolecular π–π stacking interactions between the two phenoxide groups (O1a/O1b and O2a/O2b) of the two (*R,R*)-dnsalcd^{2-} ligands. This can be attributed to each (*R,R*)-dnsalcd^{2-} ligand binding to the Gd(III) center in an overlapping mode, adopting a staggered conformation with a dihedral angle of 88.4(3)° through the co-ordinated N and O atoms.[26] Moreover, the centroid–centroid distances were measured at 3.493 and 3.558 Å, while the dihedral angles between the benzene rings were 6.6(1.0)° and 6.9 (0.8)°, indicating slight distortions in the π–π stacking interactions (Fig. S9).[44]

Photophysical properties

The photoluminescence properties of the complexes, along with those of the (*R,R*)-H$_2$dnsalcd ligand, were investigated in the solid and acetonitrile solution states at room temperature. Fig. 6 shows the emission spectra in the solid state, while Fig. 7 shows the observed f–f transitions of complexes **1–5**. For the pure chiral ligand, broad emission was detected between 450 and 600 nm, with a maximum at approximately 500 nm under 390 nm excitation.[26] The chiral ligand can generate chiral metal complexes, which may potentially induce interest-
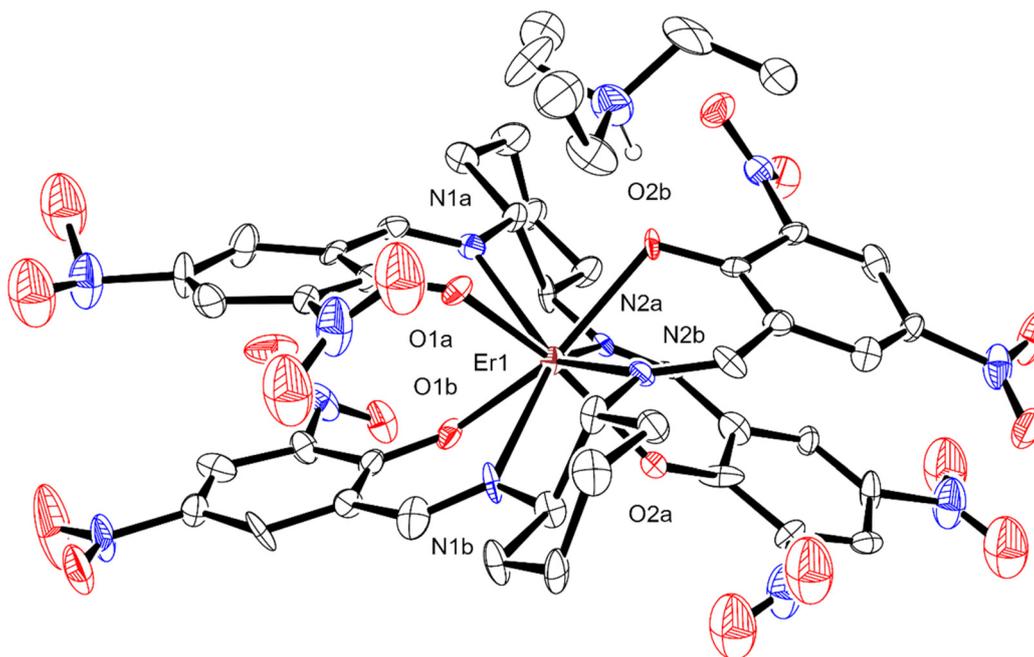
Fig. 3 ORTEP representation of complex **3**. The atoms are represented by 30% probable thermal ellipsoids. All hydrogen atoms are omitted for clarity, except for the hydrogen atom on the nitrogen of the triethylammonium cation.
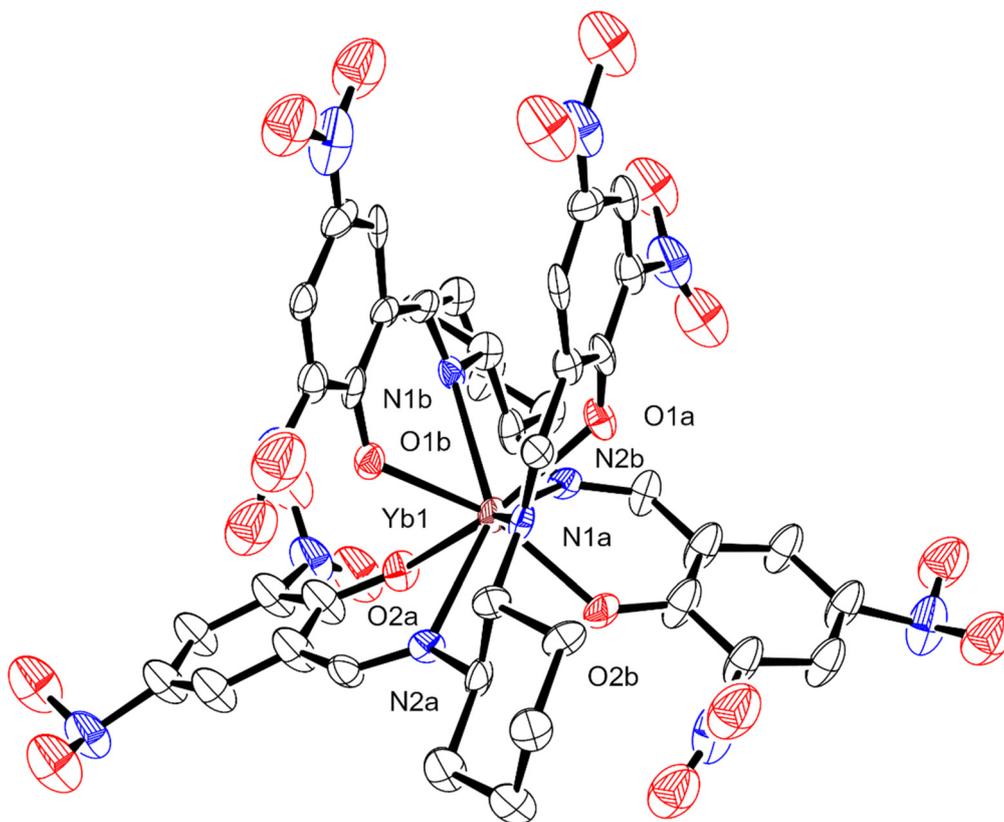

Fig. 4 ORTEP representation of complex anions of **4**. The atoms are represented by 20% probable thermal ellipsoids. All hydrogen atoms are omitted for clarity.
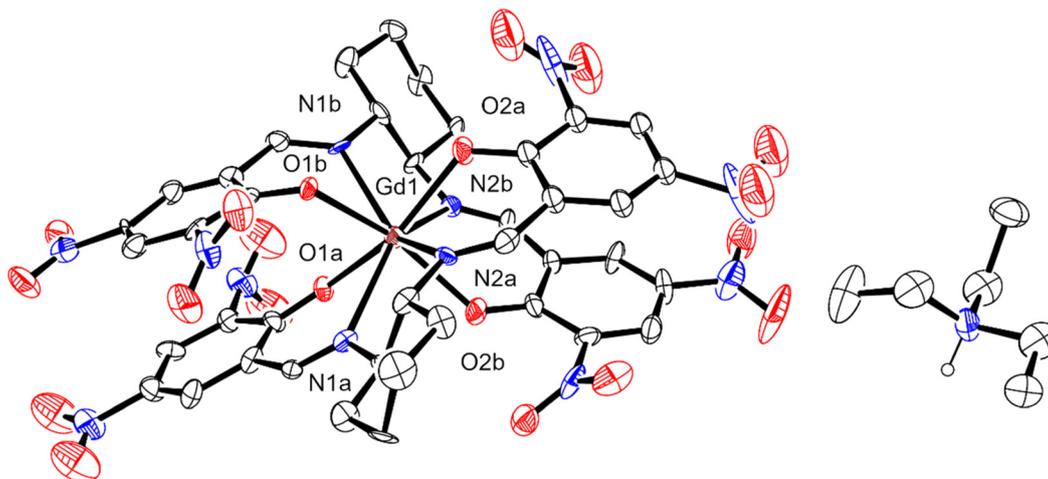
Fig. 5 ORTEP representation of complex **5**. The atoms are represented by 30% probable thermal ellipsoids. All hydrogen atoms are omitted for clarity, except for the hydrogen atom on the nitrogen of the triethylammonium cation.

ing circularly polarized luminescence. Upon excitation at 380 nm, complex **1** exhibited characteristic NIR emissions, corresponding to the $^4F_{3/2} \rightarrow ^4I_{9/2}$ (891 and 915 nm), $^4F_{3/2} \rightarrow ^4I_{11/2}$ (1059 nm), and $^4F_{3/2} \rightarrow ^4I_{13/2}$ (1330 and 1379 nm) transitions.[45] The $^4F_{3/2} \rightarrow ^4I_{9/2}$ and $^4F_{3/2} \rightarrow ^4I_{13/2}$ emission bands in **1** split into two peaks, probably attributed to the Stark splitting effect.[46] Similar splitting patterns have been previously reported,[47] which are attributed to the splitting of the emitting levels induced by ligand field effects.[48] For complex **2**, the emission spectrum showed two transition bands, attributed to the $^5F_5 \rightarrow ^5I_8$ (659 nm) and $^5F_5 \rightarrow ^5I_7$ (985 and 1057 nm) transitions upon excitation at 380 nm. For the $^5F_5 \rightarrow ^5I_7$ transition, the peak exhibited a splitting pattern, which can again be attributed to the Stark splitting effect.[47] In the spectrum of complex **3**, excitation at 380 nm led to split emission peaks at 1497, 1527, and 1552 nm, along with a very weak band at 968 nm. These peaks corresponded to the $^4I_{11/2} \rightarrow ^4I_{15/2}$ (968 nm) and $^4I_{13/2} \rightarrow ^4I_{15/2}$ (1497, 1527, and 1552 nm) transitions. For complexes **2** and **3**, the starred peaks were observed through the long pass filter at 400 nm owing to their low intensity. These complexes further exhibited weak ligand-centered emission in the 400–700 nm spectral range, indicating incomplete energy transfer from the ligand to the excited states of Ln(III) ions.[49] The emission spectrum of complex **4**, upon excitation at 380 nm, showed strong emission peaks at 977, 995, and 1017 nm, which can be attributed to the $^2F_{5/2} \rightarrow ^2F_{7/2}$ transition, with Stark splitting effects.[48] Unlike complexes **1–4**, complex **5** exhibited only a weak, broad emission band at the 400–500 nm range, with a maximum at 465 nm, which was attributed to the ligand $\pi \rightarrow \pi^*$ electronic transition. This phenomenon can be attributed to Gd(III) lacking visible photoluminescence, as its first excited state ($^6P_{7/2}$) lies ~32 000 cm^{-1} above its ground state.[50]

Fig. 8 shows the emission spectra of complexes **1–4** in the MeCN solution. No emission was observed for the chiral Schiff base ligand and complex **5**, owing to solvent-induced quench-

ing, which resulted from ligand–solvent interactions.[52] For complex **1**, the emission spectrum showed the same pattern as the solid state, exhibiting three characteristic NIR emission peaks: $^4F_{3/2} \rightarrow ^4I_{9/2}$ (887 and 918 nm), $^4F_{3/2} \rightarrow ^4I_{11/2}$ (1060 and 1083 nm), and $^4F_{3/2} \rightarrow ^4I_{13/2}$ (1331 nm) transitions. For complex **2**, three sets of emission bands were observed again, though with significantly reduced intensities compared to those observed in the solid state. The Stark splitting emission peaks at 612, 657, and 701 nm were attributed to $^5F_5 \rightarrow ^5I_8$ transitions, while the broad splitting peaks at 862 and 980 nm corresponded to the $^5F_5 \rightarrow ^5I_7$ transition.[47b] A weak band was also observed at 1186 nm, corresponding to the $^5I_6 \rightarrow ^5I_8$ transition. Complex **3** exhibited a characteristic $^4I_{13/2} \rightarrow ^4I_{15/2}$ transition band of the Er(III) ion at 1527 nm, with a shoulder at *ca.* 1561 nm with a lower intensity than that in the solid state. The weak $^4I_{11/2} \rightarrow ^4I_{15/2}$ transition band disappeared in the solution state. Conversely, the emission spectrum of complex **4** exhibited an intense peak in the 900–1100 nm range, with a maximum at 995 nm, corresponding to the $^2F_{5/2} \rightarrow ^2F_{7/2}$ transition.[48] This behavior demonstrates that the (*R,R*)-dnsalcd^{2-} ligand effectively sensitizes Nd(III) and Yb(III) ions through an efficient antenna effect in the solid state and MeCN solution. These complexes are comparable to those of Eu(III) complexes reported by our group.[26] Moreover, NIR emissions were observed in the Ho(III) and Er(III) complexes, which are quite unusual compared to those with the Tb(III) complexes.[26] In the case of the Tb(III) complexes, the presence of two intramolecular π–π stacking interactions appears to quench or hinder the energy transfer process, leading to suppressed lanthanide-centered emission. Therefore, it was initially expected that the Ho(III) and Er(III) complexes would not exhibit energy transfer from the ligand to the Ln(III) ions due to the presence of two intramolecular π–π stacking interactions. Unexpectedly, however, NIR emissions were observed in both complexes, albeit not intense. These results suggest that, in contrast to the Tb(III) complexes, the two intramolecular π–π stacking interactions in
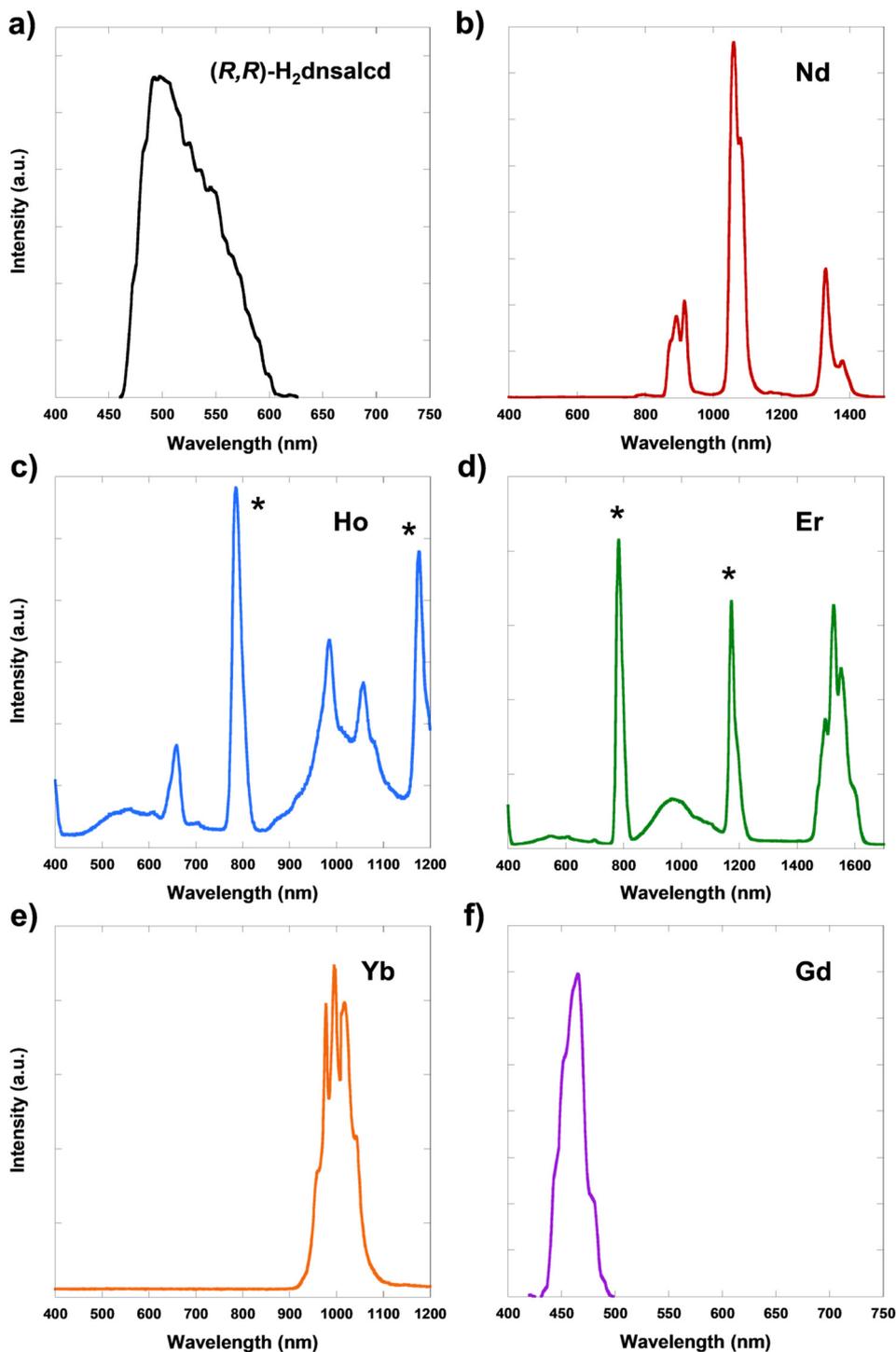
Fig. 6 Emission spectra of (a) (R,R)-H$_2$dnsalcd (λ_{ex} = 390 nm) and (b) complexes **1** (λ_{ex} = 380 nm), (c) **2** (λ_{ex} = 380 nm), (d) **3** (λ_{ex} = 380 nm), (e) **4** (λ_{ex} = 380 nm), and (f) **5** (λ_{ex} = 400 nm) in the solid state at room temperature. * indicates Rayleigh scattering peaks.

the Ho(III) and Er(III) complexes allow for a limited but measurable ligand-to-metal energy transfer. Additionally, since the NIR emissions of complexes **1–4** are observed in both the solid and solution states, intermolecular interactions can be excluded as the primary contributors to these emissions. In the case of complexes **1** and **4**, each of which exhibits a single intramolecular π–π stacking interaction, strong metal-centered emissions are observed, attributed to efficient ligand-to-metal energy transfer (*i.e.*, the antenna effect) without significant quenching. These findings indicate that the NIR emissions in complexes **1–4** are highly dependent on the number of intramolecular π–π stacking interactions.
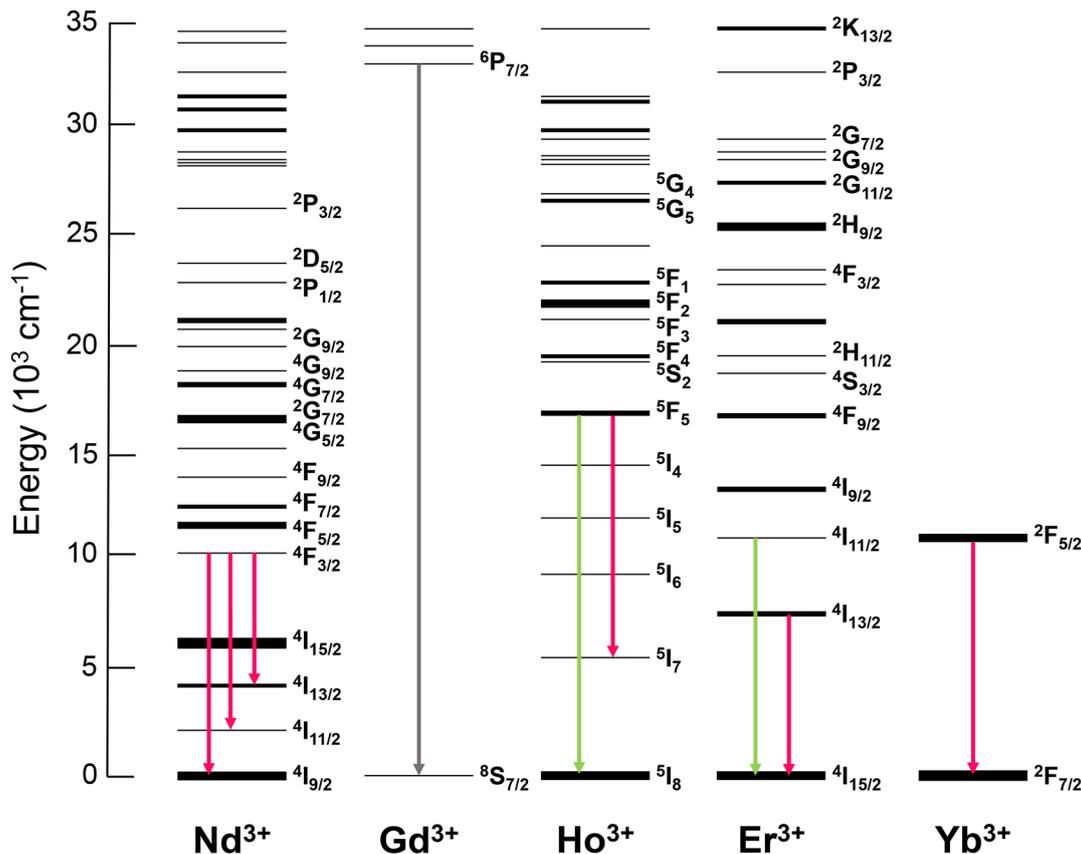
Fig. 7 Energy illustration of the observed f–f transitions in the emission spectra of complexes **1–5** in the solid state.[51]

Magnetic properties

The magnetic susceptibility data of **1–5** were obtained on solid-state samples under an applied field of 5000 Oe over a temperature range of 2–300 K using a SQUID magnetometer. Fig. 9 shows the resulting $\chi_M T$ versus T plot. At room temperature, complex **1** exhibited a $\chi_M T$ value of 1.53 emu K mol^{-1}, slightly lower than the theoretical value expected for a single, non-interacting Nd^{3+} ion (g_J = 8/11, calculated $\chi_M T$ = 1.64 emu K mol^{-1}). This difference can be attributed to the ground-state term symbol for the Nd(III) ion, ^{4}I, which splits into four different J states (^{4}I$_{9/2-15/2}$) owing to spin–orbit coupling.[53] For complex **2**, the $\chi_M T$ value at 300 K was 13.9 emu K mol^{-1}, slightly lower than that of the expected value for the ^{5}I$_8$ ground state of the Ho^{3+} ion (g_J = 5/4, calculated $\chi_M T$ = 14.07 emu K mol^{-1}). Upon cooling, $\chi_M T$ remained relatively stable until reaching 50 K, after which it sharply reduced to 3.69 emu K mol^{-1} at 2 K. This reduction can be attributed to the progressive depopulation of excited Stark sublevels influenced by ligand field effects, indicating the presence of significant magnetic anisotropy, a phenomenon frequently observed in lanthanide compounds.[54] For complex **3**, the $\chi_M T$ value at 300 K was 11.3 emu K mol^{-1}, slightly lower than the expected value for the ^{4}I$_{15/2}$ ground state of the Er^{3+} ion (g_J = 6/5, calculated $\chi_M T$ = 11.48 emu K mol^{-1}). This difference can be attributed to the ground-state term symbol for the Er(III) ion, ^{4}I, which undergoes spin–orbit coup-

ling, splitting into four different J states (^{4}I$_{9/2-15/2}$). Upon cooling, $\chi_M T$ remained relatively constant until reaching 80 K, after which it sharply reduced to 5.24 emu K mol^{-1} at 2 K. For complex **4**, the $\chi_M T$ value at 300 K was 2.52 emu K mol^{-1}, slightly lower than the expected value for the ^{2}F$_{7/2}$ ground state of the Yb^{3+} ion (g_J = 8/7, calculated $\chi_M T$ = 2.57 emu K mol^{-1}). This deviation can be attributed to the ground-state term symbol for the Yb(III) ion, ^{2}F, which undergoes spin–orbit coupling splitting into two different J states (^{2}F$_{5/2-7/2}$).[53] For complex **5**, the $\chi_M T$ value at 300 K was 8.06 emu K mol^{-1}, slightly higher than that of the calculated value for a single non-interacting Gd^{3+} ion (g_J = 7/2, calculated $\chi_M T$ = 7.87 emu K mol^{-1}). The Gd^{3+} ion exhibited an ^{8}S$_{7/2}$ ground state (4f,^{7} J = 7/2, L = 0, and S = 7/2) with no contribution from orbital angular momentum and was located approximately 10^4 cm^{-1} below the first excited state.[55] Upon cooling, $\chi_M T$ remained constant until reaching 20 K, after which it slightly reduced to 7.04 emu K mol^{-1} at 2 K. For the entire temperature range, the $\chi_M^{-1}(T)$ versus T plot adhered to the Curie–Weiss law, with θ = −0.28 K (C = 8.06 emu K mol^{-1}) for complex **5**. This is most probably attributed to antiferromagnetic interactions between the mononuclear species.

Density functional theory calculations

The emission band of complex **3** was observed at 1497, 1527, and 1552 nm upon excitation at λ_{ex} = 380 nm (Fig. 7), corres-
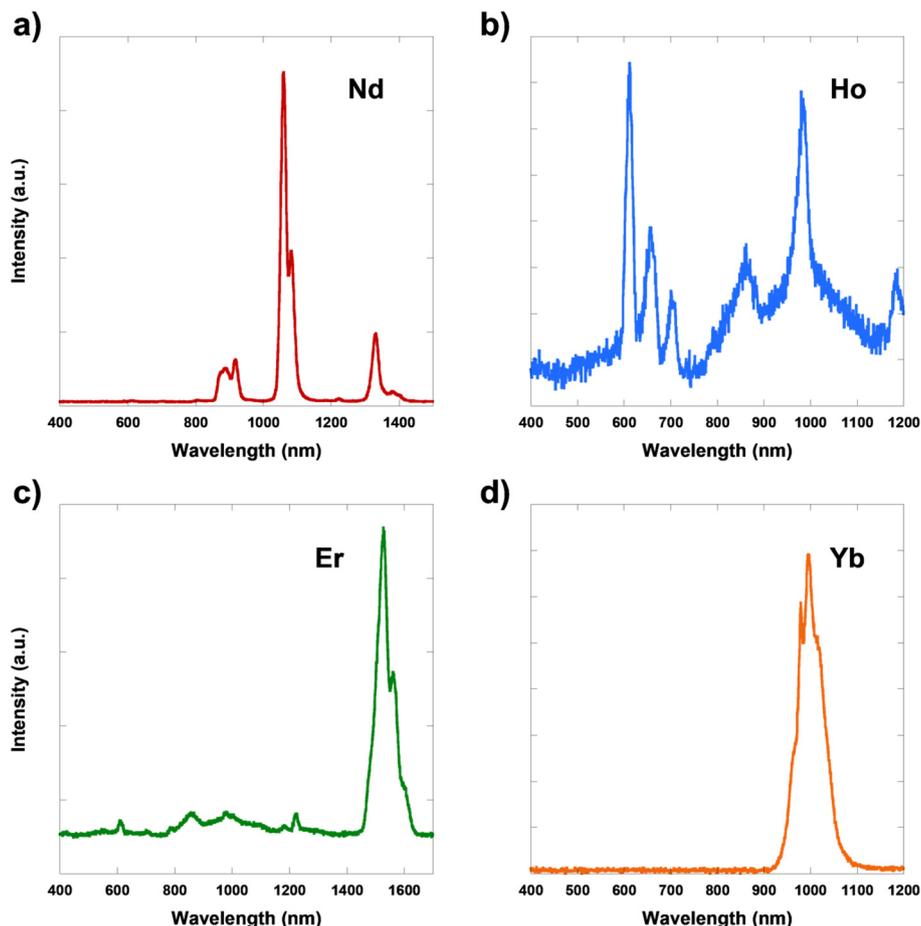
Fig. 8 Emission spectra of (a) complexes **1** (λ_{ex} = 380 nm), (b) **2** (λ_{ex} = 380 nm), (c) **3** (λ_{ex} = 380 nm), and (d) **4** (λ_{ex} = 380 nm) in MeCN solution at room temperature.
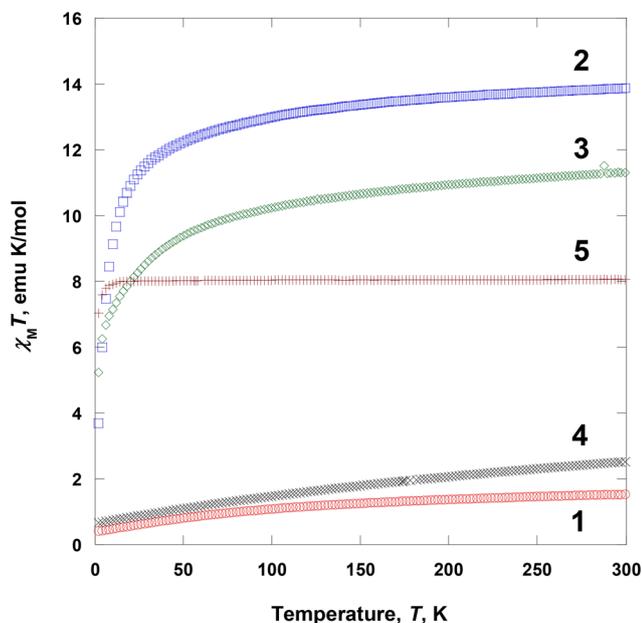

Fig. 9 Magnetic susceptibility data for complexes **1–5**, displayed as the $\chi_M T$ product.

ponding to the $^4I_{13/2} \rightarrow {}^4I_{15/2}$ transition. Thus, the DFT calculations were performed to investigate the electronic structure of the Er(III) complex. All calculations were performed using the ORCA program employing the M06-2X functional with the SARC2-ZORA-QZVP basis set for the Er atom and the ZORA-def2-TZVP basis set for all other atoms.[32,33] The calculation result showed that energy transfer occurs from the ligand to the Er(III) ion. The transition densities between the ground and excited states confirm that ligand-to-Er(III) metal energy transfer facilitates the Er(III)-centered emission. These findings suggest that the 1527 nm emission ($^4I_{13/2} \rightarrow {}^4I_{15/2}$ transition) probably occurs from a series of internal conversions from the populated $^2P_{3/2}$ level to the long-lived $^4I_{13/2}$ level (Fig. 10).[56] This mechanism differs significantly from the emission behavior observed in the Tb(III) complex.[26] In that case, the presence of two intramolecular π–π stacking interactions results in strong confinement of the π-electrons in the L+1 orbital (where L refers to the lowest unoccupied molecular orbital), thereby suppressing ligand-to-metal charge transfer upon excitation. In contrast, for complex **3**, density functional theory (DFT) calculations revealed that the transition densities of the (*R*,*R*)-dnsalcd^{2-} ligands are effectively transferred to the Er(III) ion within the complex anion, which facilitates NIR emissions.
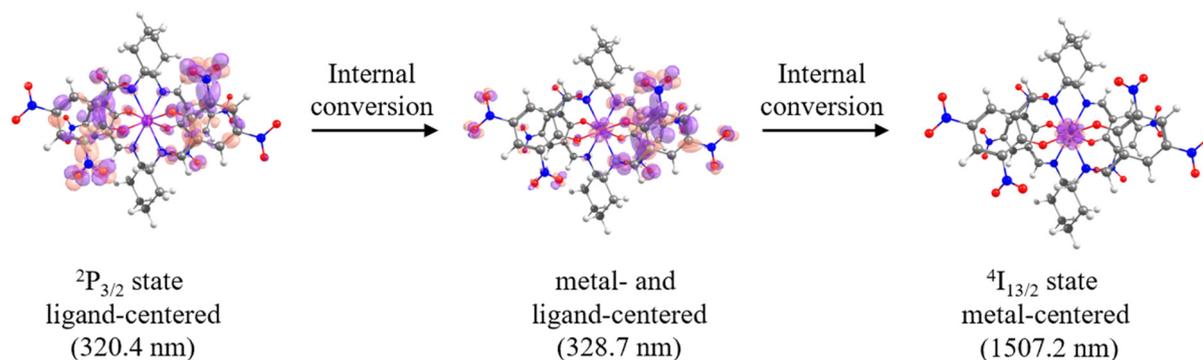
Fig. 10 Schematic representation of the energy transfer from the ligands to the metal ion in the Er(III) complex. The energies relative to the ground $^4I_{15/2}$ state are given in parentheses.

Conclusions

The synthesis and characterization of five enantiopure mononuclear complexes (teaH) [Ln((R,R)-dnsalcd)$_2$] are reported (Ln = Nd, Ho, Er, Yb, and Gd). Within this series, the chiral tetradentate ligand is coordinated to lanthanide ions in a bis-chelating mode while exhibiting two different coordination modes related to π–π interactions between benzene groups. The Nd(III) and Yb(III) complexes feature a single intramolecular π–π interaction between benzene rings, whereas the Ho(III), Er(III), and Gd(III) complexes exhibit two intramolecular π–π interactions within their complex anions. The Nd(III) and Yb(III) complexes in the solid and solution states exhibited strong NIR emissions corresponding to each metal ion within the near-infrared range, facilitated by an efficient antenna effect. In contrast, the Ho(III) and Er(III) complexes showed weak NIR emissions corresponding to each metal ion. From these results, we confirmed that the two intramolecular π–π interactions weaken the energy transfer more effectively than a single π–π interaction. Nevertheless, despite the presence of strong π–π interactions in the Ho(III) and Er(III) complexes, weak NIR emissions were still observed, contrary to previous findings. The Gd(III) complex exhibited only ligand-based emission in the solid state, whereas no emission was observed in the solution. DFT calculations confirmed that the NIR emissions in the Er(III) complex were driven by the antenna effect, which was associated with internal conversion during energy transfer from the ligands to the metal ion. Moreover, all lanthanide complexes showed paramagnetic behavior at room temperature. Upon cooling, their magnetic moments were influenced by the thermal depopulation of their respective sublevels.

Author contributions

Yuri Jeong: data curation, analysis, and writing the manuscript draft. Ngoc Tram Anh Le: data curation, analysis, and writing the manuscript draft. Jeyun Ju: DFT calculations. Iuliia Olshevskaia: DFT calculations. Daeheum Cho: DFT calculations and writing the manuscript draft. Ryuya Tokunaga: data curation and analysis. Shinya Hayami: data curation and analysis. Kil Sik Min: supervision, conceptualization, project design, and writing the manuscript draft.

Conflicts of interest

There are no conflicts to declare.

Data availability

The data supporting this article have been included as part of the SI: compound spectroscopic characterisation (XRPD, IR, UV-Vis) and SC-XRD collection and refinement details. See DOI: **https://doi.org/10.1039/d5dt01071c**.

CCDC 2448369 (**1**) and 2448371–2448373 (**3–5**) contain the supplementary crystallographic data for this paper.[57a–d]

Acknowledgements

References

1 F. Wang and X. Liu, *Acc. Chem. Res.*, 2014, **47**, 1378–1385.
2 N. Kiseleva, P. Nazari, C. Dee, D. Busko, B. S. Richards, M. Seitz and A. Turshatov, *J. Phys. Chem. Lett.*, 2020, **11**, 2477–2481.
3 T. Ahmed, A. Chakraborty, A. Paul and S. Baitalik, *Dalton Trans.*, 2023, **52**, 14027–14038.
4 A. J. Amoroso and S. J. Pope, *Chem. Soc. Rev.*, 2015, **44**, 4723–4742.

5 M. Sy, A. Nonat, N. Hildebrandt and L. J. Charbonnière, *Chem. Commun.*, 2016, **52**, 5080–5095.

6 X. Qiu, J. Xu, M. Cardoso Dos Santos and N. Hildebrandt, *Acc. Chem. Res.*, 2022, **55**, 551–564.

7 D. Parker, *Coord. Chem. Rev.*, 2000, **205**, 109–130.

8 D. Parker, J. D. Fradgley and K. L. Wong, *Chem. Soc. Rev.*, 2021, **50**, 8193–8213.

9 A. de Bettencourt-Dias, *Dalton Trans.*, 2007, **22**, 2229–2241.

10 L. Wang, Z. Zhao, C. Wei, H. Wei, Z. Liu, B. Bian and C. Huang, *Adv. Opt. Mater.*, 2019, **7**, 1801256.

11 A. Dey, P. Kalita and V. Chandrasekhar, *ACS Omega*, 2018, **3**, 9462–9475.

12 D. N. Woodruff, R. E. P. Winpenny and R. A. Layfield, *Chem. Rev.*, 2013, **113**, 5110–5148.

13 R. J. Blagg, L. Ungur, F. Tuna, J. Speak, P. Comar, D. Collison, W. Wernsdorfer, E. J. L. McInnes, L. F. Chibotaru and R. E. P. Winpenny, *Nat. Chem.*, 2013, **5**, 673–678.

14 J. C. G. Bünzli, S. Comby, A. S. Chauvin and C. D. Vandevyver, *J. Rare Earths*, 2007, **25**, 257–274.

15 H. Suzuki, *J. Photochem. Photobiol., A*, 2004, **166**, 155–161.

16 J. C. G. Bünzli, *Chem. Rev.*, 2010, **110**, 2729–2755.

17 B. M. Van Der Ende, L. Aarts and A. Meijerink, *Phys. Chem. Chem. Phys.*, 2009, **11**, 11081–11095.

18 Y. Ning, Y.-W. Liu, Y.-S. Meng and J.-L. Zhang, *Inorg. Chem.*, 2018, **57**, 1332–1341.

19 T. N. Nguyen, G. Capano, A. Gładysiak, F. M. Ebrahim, S. V. Eliseeva, A. Chidambaram, B. Valizadeh, S. Petoud, B. Smit and K. C. Stylianou, *Chem. Commun.*, 2018, **54**, 6816–6819.

20 D. Davis, A. J. Carrod, Z. Guo, B. M. Kariuki, Y.-Z. Zhang and Z. Pikramenou, *Inorg. Chem.*, 2019, **58**, 13268–13275.

21 Y. Gil, R. C. de Santana, A. S. S. de Camargo, L. G. Merízio, P. F. Carreño, P. Fuentealba, J. Manzur and E. Spodine, *Dalton Trans.*, 2023, **52**, 3158–3168.

22 A. Fanourakis and R. J. Phipps, *Chem. Sci.*, 2023, **14**, 12447–12476.

23 (*a*) F.-X. Xu, Y.-L. Li, X.-Q. Wei, D. Shao, L. Shi, H.-Y. Wei and X.-Y. Wang, *Dalton Trans.*, 2023, **52**, 5575–5586; (*b*) Z. Zhu, C. Zhao, T. Feng, X. Liu, X. Ying, X.-L. Li, Y.-Q. Zhang and J. Tang, *J. Am. Chem. Soc.*, 2021, **143**, 10077–10082.

24 M. Tsurui, R. Takizawa, Y. Kitagawa, M. Wang, M. Kobayashi, T. Taketsugu and Y. Hasegawa, *Angew. Chem., Int. Ed.*, 2024, **63**, e202405584.

25 (*a*) J. Liu, W. Song, H. Niu, Y. Lu, H. Yang, W. Li, Y.-z. Zhao and Z. Miao, *Inorg. Chem.*, 2024, **63**, 18429–18437; (*b*) Y. Tang, M. Jian, B. Tang, Z. Zhu, Z. Wang and Y. Liu, *Inorg. Chem. Front.*, 2024, **11**, 2039–2048; (*c*) T. Feng, R. Cai, Z. Zhu, Q. Zhou, A. Sickinger, O. Maury, Y. Guyot, A. Bensalah-Ledoux, S. Guy, B. Baguenard, B. Le Guennic and J. Tang, *Chem. – Eur. J.*, 2025, **31**, e202500910.

26 S. Jeon, Y. Jeong, L. N. T. Anh, J. Ju, D. Cho, Y. J. Jang, R. Tokunaga, S. Hayami and K. S. Min, *J. Ind. Eng. Chem.*, 2023, **128**, 275–285.

27 G. Shen, F. Gou, J. Cheng, X. Zhang, X. Zhou and H. Xiang, *RSC Adv.*, 2017, **7**, 40640–40649.

28 G. A. Bain and J. F. Berry, *J. Chem. Educ.*, 2008, **85**, 532–536.

29 A. Verma, M. K. Tiwari, N. Subba and S. Saha, *J. Photochem. Photobiol., A*, 2022, **433**, 114130.

30 E. G. Hohenstein, S. T. Chill and C. D. Sherrill, *J. Chem. Theory Comput.*, 2008, **4**, 1996–2000.

31 Z. Zhou, J. McNeely, J. Greenough, Z. Wei, H. Han, M. Rouzières, A. Y. Rogachev, R. Clérac and M. A. Petrukhina, *Chem. Sci.*, 2022, **13**, 3864–3874.

32 D. Aravena, F. Neese and D. A. Pantazis, *J. Chem. Theory Comput.*, 2016, **12**, 1148–1156.

33 F. Weigend and R. Ahlrichs, *Phys. Chem. Chem. Phys.*, 2005, **7**, 3297–3305.

34 *APEX3, v2019.1-0*, Bruker, Madison, WI, USA, 2019.

35 (*a*) *SADABS, version 2016/2*, Bruker-AXS, Madison, WI, USA, 2016; (*b*) L. Krause, R. H. Irmer, G. M. Sheldrick and D. Stalke, *J. Appl. Crystallogr.*, 2015, **48**, 3–10.

36 G. M. Sheldrick, *SHELXT*, Universität Göttingen, Göttingen, Germany, 2014.

37 G. M. Sheldrick, *Acta Crystallogr., Sect. A:Found. Adv.*, 2015, **C71**, 3–8.

38 (*a*) P. van der Sluis and A. L. Spek, *Acta Crystallogr., Sect. A: Found. Crystallogr.*, 1990, **A46**, 194–201; (*b*) A. L. Spek, *Acta Crystallogr., Sect. A:Found. Adv.*, 2015, **C71**, 9–18.

39 A. S. Smirnov, A. S. Kritchenkov, N. A. Bokach, M. L. Kuznetsov, S. I. Selivanov, V. V. Gurzhiy, A. Roodt and V. Y. Kukushkin, *Inorg. Chem.*, 2015, **54**, 11018–11030.

40 S. K. Sharma, T. Behm, T. Köhler, J. Beyer, R. Gloaguen and J. Heitmann, *Crystals*, 2020, **10**, 593.

41 K. Binnemans, R. V. Deun, C. Görller-Walrand, S. R. Collinson, F. Martin, D. W. Bruce and C. Wickleder, *Phys. Chem. Chem. Phys.*, 2000, **2**, 3753–3757.

42 I. Pospieszna-Markiewicz, M. A. Fik-Jaskółka, Z. Hnatejko, V. Patroniak and M. Kubicki, *Molecules*, 2022, **27**, 8390.

43 J. C. Slater, *J. Chem. Phys.*, 1964, **41**, 3199–3204.

44 (*a*) M. Mantina, A. C. Chamberlin, R. Valero, C. J. Cramer and D. G. Truhlar, *J. Phys. Chem. A*, 2009, **113**, 5806; (*b*) A. R. Jeong, J. W. Shin, J. H. Jeong, S. Jeoung, H. R. Moon, S. Kang and K. S. Min, *Inorg. Chem.*, 2020, **59**, 15987.

45 Y. Hasegawa, Y. Wada and S. Yanagida, *J. Photochem. Photobiol., C*, 2004, **5**, 183–202.

46 (*a*) L. Zhang, T. Xue, D. He, M. Guzik and G. Boulon, *Opt. Express*, 2015, **23**, 1505–1511; (*b*) B. Yang, X. Liu, X. Wang, J. Zhang, L. Hu and L. Zhang, *Opt. Lett.*, 2014, **39**, 1772–1774.

47 Z. Li, J. Yu, L. Zhou, R. Deng and H. Zhang, *Inorg. Chem. Commun.*, 2009, **12**, 151–153.

48 (*a*) J. A. Jiménez, R. Amesimenu and M. Thomas, *J. Phys. Chem. B*, 2024, **128**, 2995–3003; (*b*) M. A. Katkova, A. P. Pushkarev, T. V. Balashova, A. N. Konev, G. K. Fukin, S. Y. Ketkov and M. N. Bochkarev, *J. Mater. Chem.*, 2011, **21**, 16611–16620.

49 (*a*) I. Pospieszna-Markiewicz, M. A. Fik-Jaskółka, Z. Hnatejko, V. Patroniak and M. Kubicki, *Molecules*, 2022,

27, 8390; (*b*) J. Choo, A. R. Jeong, H. Yeo, S. Hayami and K. S. Min, *J. Mol. Struct.*, 2020, **1206**, 127726.

50 J. F. Greisch, M. E. Harding, B. Schäfer, M. Ruben, W. Klopper, M. M. Kappes and D. Schooss, *J. Phys. Chem. Lett.*, 2014, **5**, 1727–1731.

51 J.-C. G. Bünzli and C. Piguet, *Chem. Soc. Rev.*, 2005, **34**, 1048–1077.

52 T. J. Penfold, S. Karlsson, G. Capano, F. A. Lima, J. Rittmann, M. Reinhard, M. H. Rittmann-Frank, O. Braem, E. Baranoff, R. Abela, I. Tavernelli, U. Rothlisberger, C. J. Milne and M. Chergui, *J. Phys. Chem. A*, 2013, **117**, 4591–4601.

53 E. R. Martí, A. B. Canaj, T. Sharma, A. Celmina, C. Wilson, G. Rajaraman and M. Murrie, *Inorg. Chem.*, 2022, **61**, 9906–9917.

54 P. Wytrych, J. Utko, M. Stefanski, J. Kłak, T. Lis and Ł. John, *Inorg. Chem.*, 2023, **62**, 2913–2923.

55 R. C. A. Vaz, I. O. Esteves, W. X. C. Oliveira, J. Honorato, F. T. Martins, L. F. Marques, G. L. dos Santos, R. O. Freire, L. T. Jesus, E. F. Pedroso, W. C. Nunes, M. Julve and C. L. M. Pereira, *Dalton Trans.*, 2020, **49**, 16106–16124.

56 A. Upadhyay, K. R. Vignesh, C. Das, S. K. Singh, G. Rajaraman and M. Shanmugam, *Inorg. Chem.*, 2017, **56**, 14260–14274.

57 (*a*) Y. Jeong, N. T. A. Le, J. Ju, I. Olshevskaia, D. Cho, R. Tokunaga, S. Hayami and K. S. Min, CCDC 2448369: Experimental Crystal Structure Determination, 2025, DOI: **10.5517/ccdc.csd.cc2n5qn7**; (*b*) Y. Jeong, N. T. A. Le, J. Ju, I. Olshevskaia, D. Cho, R. Tokunaga, S. Hayami and K. S. Min, CCDC 2448371: Experimental Crystal Structure Determination, 2025, DOI: **10.5517/ccdc.csd.cc2n5qq9**; (*c*) Y. Jeong, N. T. A. Le, J. Ju, I. Olshevskaia, D. Cho, R. Tokunaga, S. Hayami and K. S. Min, CCDC 2448372: Experimental Crystal Structure Determination, 2025, DOI: **10.5517/ccdc.csd.cc2n5qrb**; (*d*) Y. Jeong, N. T. A. Le, J. Ju, I. Olshevskaia, D. Cho, R. Tokunaga, S. Hayami and K. S. Min, CCDC 2448373: Experimental Crystal Structure Determination, 2025, DOI: **10.5517/ccdc.csd.cc2n5qsc**.